Nuclear Science and Techniques (2025) 36:154
https://doi.org/10.1007/s41365-025-01722-3

Investigating the pion emission source in pp collisions using the AMPT model with subnucleon structure

Dong-Fang Wang[1,2] · **Mei-Yi Chen**[1,2] · **Yu-Gang Ma**[1,2] · **Qi-Ye Shou**[1,2] · **Song Zhang**[1,2] · **Liang Zheng**[2,3]

Received: 26 December 2024 / Revised: 22 January 2025 / Accepted: 26 January 2025 / Published online: 9 June 2025

Abstract

The measurement of momentum correlations of identical pions serves as a fundamental tool for probing the space-time properties of a particle-emitting source created in high-energy collisions. Recent experimental results have shown that in pp collisions, the size of the one-dimensional primordial source depends on the transverse mass (m_{T}) of the hadron pairs, following a common scaling behavior similar to that observed in Pb–Pb collisions. In this study, a systematic analysis of the π- π source and correlation functions was performed using the multiphase transport model (AMPT) to understand the properties of the emitting source created in high-multiplicity pp collisions at $\sqrt{s} = 13\,\mathrm{TeV}$. The m_{T}-scaling behavior and pion emission source radii measured by the ALICE experiment can be described well by a model with a subnucleon structure. This work sheds new light on the effective size of the π-π emission source and the study of intensity interferometry in small systems using a transport model.

Keywords Femtoscopy · Emission source · m_{T}-scaling · AMPT

1 Introduction

The correlation between two particles at a small relative momentum, known as femtoscopy, provides a unique method for directly probing the properties of particle emissions and subsequent final-state interactions (FSI) [1]. To qualify the strength of the correlation, the two-particle correlation function $C(k^*)$ is theoretically defined using the Koonin–Pratt equation [1, 2]

$$C(k^*) = \int S(\mathbf{r}^*)|\Psi(\mathbf{r}^*, \mathbf{k}^*)|\mathrm{d}^3 r^*, \tag{1}$$

where $r^* = |\mathbf{r}_1^* - \mathbf{r}_2^*|$ and $k^* = |\mathbf{p}_1^* - \mathbf{p}_2^*|/2$ represent the relative distance and momentum, respectively, between two particles in the pair of rest frames (denoted by $*$). By definition, $C(k^*)$ consists of two main components: the emission source function $S(\mathbf{r}^*)$, which describes the probability of producing two particles at a relative distance $\mathbf{r}^*$, and the wave function $\Psi(\mathbf{r}^*, \mathbf{k}^*)$, which is an asymptotic form of the combination of the outgoing plane waves and scattered waves [3]. Typically, assuming that the emission source is known (e.g., an isotropic Gaussian), one can extract the interaction between two particles of interest, often through Lednický–Lyuboshits parameterization [4] quantified by the scattering length and

---

This work was supported by the National Natural Science Foundation of China (Nos. 12061141008, 12147101, and 12322508) and the Science and Technology Commission of Shanghai Municipality (23590780100). LZ acknowledges the support of the Fundamental Research Funds for the Central Universities, China University of Geosciences (Wuhan), with No. G1323523064.

✉ Qi-Ye Shou
shouqiye@fudan.edu.cn

Yu-Gang Ma
mayugang@fudan.edu.cn

Liang Zheng
zhengliang@cug.edu.cn

[1] Key Laboratory of Nuclear Physics and Ion-beam Application (MOE), Institute of Modern Physics, Fudan University, Shanghai 200433, China

[2] Shanghai Research Center for Theoretical Nuclear Physics, NSFC and Fudan University, Shanghai 200438, China

[3] School of Mathematics and Physics, China University of Geosciences (Wuhan), Wuhan 430074, China

effective range [5], which has been successfully applied to various measurements in heavy-ion collisions (HICs) [6–9].

Alternatively, with the known interaction, the spatial extent and the duration of the emission source can be investigated through the interference of identical particles (e.g., pions) [10, 11]. Such intensity interferometry in HICs is commonly known as Hanbury-Brown–Twiss analysis (HBT) [12, 13]. The range of the strong interaction between the two charged pions is expected to be approximately 0.2 fm [14], and the scattering length $a_0^{I=2}$ is -0.0444 fm [15, 16], indicating that the effect of the strong interaction on the π-π correlation function should be negligible. Consequently, the π-π interaction is primarily dominated by long-range Coulomb forces and the Bose–Einstein effect (quantum statistics).

Femtoscopic studies show that, in both pp and Pb–Pb collisions, the source size distinctly decreases as a function of the pair's transverse mass m_{T}, defined as $m_{\mathrm{T}} = \sqrt{\langle k_{\mathrm{T}}\rangle^2 + m^2}$, where $k_{\mathrm{T}} = \left|\mathbf{p}_{\mathrm{T},1} + \mathbf{p}_{\mathrm{T},2}\right|/2$ is the transverse momentum of the pair at rest frame and m is the particle mass. This phenomenon, commonly referred to as m_{T}-scaling, has been observed for both identical mesons and baryons, such as pions, kaons, and protons [7, 17], and for nonidentical particles, such as p- Λ [18] and K-p [17]. In Pb–Pb collisions, scaling is typically attributed to the collective expansion of the system, that is, radial flow [1], which can be described well by (3+1)D-dimensional hydrodynamic models [19–23]. In pp collisions, the range of strong interactions ($\approx 1{-}2$ fm) is comparable to the source size ($1{-}3$ fm) and hadronization is believed to occur on a similar timescale for all hadrons, which would lead to the corresponding m_{T}-scaling. However, unexpectedly strong collectivity has been experimentally observed in pp collisions in recent years [24–27], and its origin is not fully understood. Hence, emission sources and m_{T} -scaling in pp collisions have become even more intriguing and gained considerable attention.

In addition to phenomenological models traditionally used in HICs for femtoscopic studies, such as EPOS [28], UrQMD [29–34], HIJING [35], CRAB [36] and others [37–42], CECA [43] offers a novel numerical approach to investigate the emission source. However, a comprehensive description that reasonably aligns collective flow with femtoscopy remains incomplete for pp collisions, although the former is recognized as the driving force behind the latter. It should be noted that the collective flow in pp collisions can be successfully reproduced by a multiphase transport model (AMPT) implementing subnucleon geometry, as demonstrated in recent studies [44–46]. This configuration, which incorporates the constituent-quark assumption for protons, can generate a large initial spatial eccentricity, leading to a significant long-range azimuthal correlation during pp collisions. Therefore, it is crucial and natural to further explore whether such a framework is valid for revealing space-time characteristics. This work presents the first attempt to model the correlation function, emission source, and m_{T}-scaling in high-multiplicity pp collisions at $\sqrt{s} = 13$ TeV using the state-of-the-art AMPT.

The remainder of this paper is organized as follows. In Sect. 2, we provide a short introduction to the model and key parameters. This is followed by an overview of the femtoscopic methodology, which includes the source function and framework used to provide an accurate FSI of pion pairs. In Sect. 3, the impact of various physical factors, such as the parton rescattering cross-section σ_{p}, initial partonic distribution, short-lived resonances, and hadron rescattering processes, on the emission source is examined. Most importantly, the dependence of m_{T} on the π-π source size is investigated. Finally, a summary is presented in Sect. 4.

2 Model and methodology

2.1 AMPT model

The AMPT hybrid dynamic model [47, 48], which includes both partonic and hadronic scattering, has been used extensively to study various key features of HICs, such as hadron production [49, 50], collectivity [51–54] and phase transitions [55]. In recent years, this model has been extended to small systems, such as pp and p–Pb collisions [45]. AMPT consists of four key components to simulate the collision process: the initial conditions generated using the Heavy Ion Jet Interaction Generator (HIJING) model [56, 57]; the partonic interactions described by Zhang's Parton Cascade (ZPC) model [58]; the hadronization process, which occurs through either Lund string fragmentation or a coalescence model; and the hadronic rescatterings modeled by A Relativistic Transport (ART) model [59]. The model has two versions: (1) the string-melting version, in which a partonic phase is generated from excited strings in the HIJING model and a simple quark coalescence model combines partons into hadrons, and (2) the default version, which proceeds only through a pure hadron gas phase.

This work is based on the AMPT with the string-melting configuration, incorporating subnucleon geometry when sampling the initial transverse positions of parton sources before converting them into constituent quarks (denoted by "3 quarks"). This special tuning method introduced in Ref. [44] can successfully reproduce the spectra and elliptic flows of the identified hadrons in pp collisions at TeV scale. Details of the initial partonic distribution are presented in Sec. 3. To illustrate the effects of the parton rescattering process, the value of σ_{p} in the ZPC was set to 1.5 mb and 10 mb, where 1.5 mb is typically applied to larger systems [60].

The high-multiplicity events in the AMPT were selected based on the number of charged particles in the pseudorapidity regions $-3.7 < \eta < -1.7$ and $2.8 < \eta < 5.1$ corresponding to the acceptance of the ALICE V0 detector. Additionally, an average multiplicity of approximately 30 charged particles was considered in the pseudorapidity interval $|\eta| < 0.5$, following the event classification scheme used in ALICE pp collisions [61]. Using the particle selection criteria from the ALICE measurements [17], charged pions were selected in the pseudorapidity range $|\eta| < 0.8$ within the transverse momentum (p_{T}) range of $0.14 - 4.0$ GeV/c.

2.2 The correlation function and emission source

The correlation function is expressed in Eq. (1). In this study, assuming that the emission source was identical in all spatial directions, a single scalar k^* was considered instead of the general three-dimensional $\mathbf{k}*$. The source function $S(r^*)$ describes the probability of producing two particles at a relative distance r^* and is commonly modeled using a Gaussian profile:

$$S(r^*) = \frac{1}{\left(2\pi R_{ab}^2\right)^{3/2}} \exp\left(-\frac{r^{*2}}{2R_{ab}^2}\right). \tag{2}$$

Here, R_{ab} represents the general expression for the two-particle source radius of the a-b pair. For identical particle pairs ($a = b$), this is simplified to $R_{aa} = \sqrt{2}R_a$. Note that r^* denotes the relative distance between the particles in specific pairs, whereas R typically represents the variance in the distribution, reflecting the overall characteristics of the r^* distribution contributed by many pairs. A two-component source consisting of a core from primary particles and a halo formed by resonance decay has been used to describe the Bose–Einstein correlations between identical pions in HICs [62]. This study follows the same nomenclature. In additional, this "resonance halo," arising from short-lived, strongly decaying resonances ($c\tau \leq 5$ fm), significantly increases the source size by introducing exponential tails to the source function of p-p and π-π, as observed in recent pp collisions measurements [17, 18]. R_{core} represents the core Gaussian source radius, and R_{eff} represents the effective Gaussian source radii that contain the resonance effect. For the previous measurements in Pb–Pb [7], R_{inv} can also be used to determine the source radius of identical pairs, called the single-particle source radius, which is the same as R_a. In this study, the observed core source radius π-π is expressed as R_{core}, where $R_{\mathrm{core}} = R_\pi = R_{\pi\pi}/\sqrt{2}$. Previous studies [63–65] did not explicitly account for the effects of resonances; instead, they used a Cauchy/exponential-type source parameterization [66],

$$S(r^*) = \frac{1}{\pi^2}\frac{R_{\mathrm{exp}}}{(R_{\mathrm{exp}}^2 + r^{*2})^2}, \tag{3}$$

where the Cauchy source size is denoted by R_{exp}. In the absence of angular dependence, the probability of emitting two particles at a given r^* can be obtained by a simple integration over the solid angle $S_{4\pi}(r^*) = 4\pi r^{*2}S(r^*)$. From a different perspective, Hanbury-Brown–Twiss (HBT) interferometry measurements [67, 68] indicate that the shape of the correlation function obtained in a longitudinally comoving system (LCMS) is different in the R_{long}, R_{side}, and R_{out} directions.

However, for simplicity, the results of this study were based on the isotropic Gaussian source shown in Eq. 2. Because of the fundamental assumptions in the Lednický parameterization [5], the effective range expansion of the scattering amplitude is not valid for small systems, particularly pp collisions [69]. Therefore, the two-particle wave function is obtained using the "Correlation Analysis Tool using the Schrödinger Equation" (CATS) framework [70], which numerically solves the Schrödinger equation for a configurable interaction potential. In this study, the phase space of the charged particles (positions and momenta) is provided by the AMPT model, whereas the CATS framework is used to accurately account for the FSI of the pairs to construct the π-π correlation function.

With a time step of 0.2 fm/c in the AMPT computational framework, the particle generated earlier must propagate along its momentum for the time difference between the pair to satisfy the equal emission time condition, as illustrated

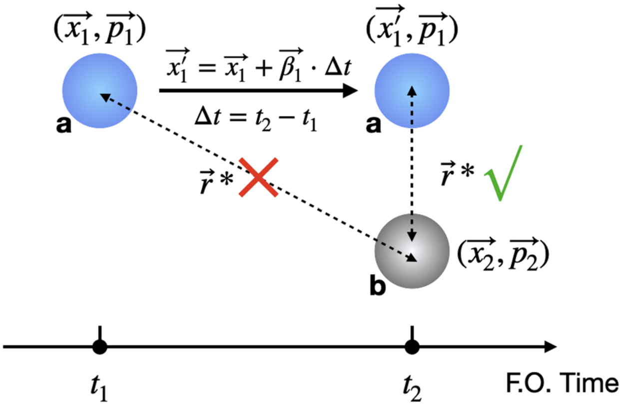

Fig. 1 (Color online) Illustration of the modification of the coordinate $\vec{x_1}$ to $\vec{x_1'}$ for particle a (blue disk), which is generated at time t_1, due to the different freeze-out time compared to particle b (gray disk), generated at time t_2, in pairing the two particles based on the AMPT framework. The coordinate system is defined by the rest frame of the two particles and is consistent with Eq. (1), where $\vec{r^*}$ represents their relative distance (dash-dotted lines)

in Fig. 1. Consider a pair of particles labeled a and b. The particle a, represented as a blue disk, is emitted at freeze-out (F.O.) time t_1 with position and momentum $(\vec{x}_1, \vec{p}_1)$, earlier than the particle b, represented as a gray disk, which is emitted at time t_2 with $(\vec{x}_2, \vec{p}_2)$. Under equal emission time conditions, the particle a must propagate over a certain distance $\Delta\vec{x}_1 = \vec{\beta}_1 \cdot (t_2 - t_1)$ along the direction of its velocity $\vec{\beta}_1$. The distance of the pair r^* is then calculated using $(\vec{x}'_1, \vec{p}_1)$ and $(\vec{x}_2, \vec{p}_2)$, where $\vec{x}'_1 = \vec{x}_1 + \Delta\vec{x}_1$. In this model, no difference is expected between π^+ and π^-. Therefore, in the following text, the term π-π refers to a combination of π^+-π^+ and π^--π^- pairs.

3 Results and discussion

3.1 Effect of initial partonic distribution

The initial partonic distribution during the ZPC stage played a crucial role in determining the source function. To investigate this effect, three initial partonic patterns were considered, as shown in panel (a) of Fig. 2. Partons can be generated from (1) the overlapping area of the quarks (colored disks) inside the protons [44], mimicking the constituent-quark scenario, and (2) three fixed black points along the impact parameter direction b, corresponding to the centers of two colliding protons and the center of the impact parameter. In the model coordinate system, these are located at $x = -b/2$, $x = b/2$ and $x = 0$. This is the intrinsic setting of AMPT, although it may not be entirely realistic; and (3) the geometrical center of the event ($x = 0$), which serves as a reference for cross-checking the extreme case. These three settings are labeled as “3 quarks”, “Normal”, and “Point-like”, respectively, in this work.

In Fig. 3, the m_{T} integrated source functions of the π-π pairs in femtoscopy region ($k^* < 250$ MeV/c) for the three initial configurations are represented. The results before and after ART are represented by solid and dashed lines, respectively. Because the coalescence mechanism from partons to hadrons is identical for any initial partonic configuration, discrepancies in the source function before the ART stage can arise only from differences in the initial partonic distribution. The mean relative distance $\langle r^* \rangle$ of the source function is a convenient variable for comparing the different distributions. Qualitative observations of the source function shape show that, before the ART stage, the source aligns with a Gaussian with $R_\pi \approx 0.65$ fm, 0.41 fm, and 0.33 fm and $\langle r^* \rangle \approx 1.58$ fm, 0.98 fm, and 0.77 fm for three initial patterns, respectively. In contrast, after the ART stage, the source matches a Cauchy with $R_{\mathrm{exp}} \approx 2.22$ fm, 2.13 fm, and 1.93 fm and $\langle r^* \rangle \approx 4.15$ fm, 3.94 fm, and 3.60 fm. As mentioned in Sect. 2, the Cauchy source is considered an effective representation of the genuine source, with its exponential tail primarily originating from the resonances, as investigated in the following sections. In the “3 quarks” model, hadrons can only be generated from the overlap region of the binary constituent quark, as shown in sub-panel (a) of Fig. 2. This overlap has the potential to contribute to a more widely dispersed distribution in the coordinate space compared with the other two initial distributions, resulting in a broader source function.

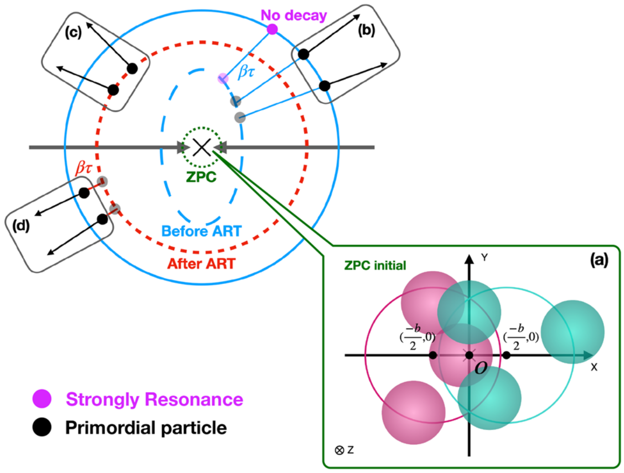

Fig. 2 (Color online) Schematic view of the AMPT evolution from the space-time perspective. (a) illustrates the initial partonic distribution. (b) and (d) depict the core source radii for a pair of primordial hadrons, boosted before and after the ART stage, respectively, with an emission time parameter τ and each particle’s velocity $\vec{\beta}$. (c) is the same as (d) but with $\tau = 0$. The figure is inspired by [43]

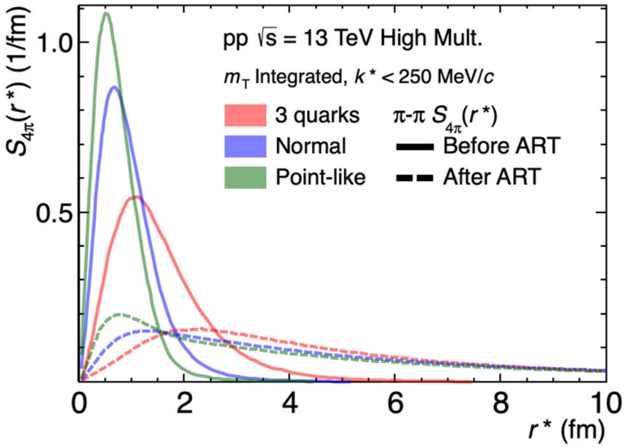

Fig. 3 (Color online) π-π source functions before and after the ART stage from three initial partonic distributions. See the text for details

3.2 Fitting source function in different k_T intervals

The correlation function is commonly divided into m_T intervals to ensure a consistent number of pairs in the femtoscopic signal region (e.g., $k^* < 250$ MeV/c). Here, the π-π source function in the AMPT is also divided into different k_T (m_T) intervals, following Ref. [17], with k_T ranges 0.15−0.3, 0.3−0.5, 0.5−0.7, 0.7−0.9, and 0.9−1.5 GeV/c. The general explanation for the m_T-scaling observed in several different experiments [7, 17, 18] and simulations [19, 20, 43] is that a higher m_T corresponds to earlier particle generation, leading to a smaller source radius. Conversely, as m_T decreases, low-momentum particles are more likely to be produced in a more homogeneous region [1], thereby contributing to a larger source. In Fig. 4, the source functions for the two example k_T intervals are represented by red and blue lines, respectively, with the before- and after-ART stages shown by solid crosses and circles, respectively.

Gaussian and Cauchy source functions were used to fit the source distributions before and after the ART stage at two k_T intervals, represented by the solid and dashed lines, respectively. This fitting yields the radii $R_\pi = 0.78$ fm and 0.63 fm and $R_{\mathrm{exp}} = 3.09$ fm and 1.96 fm, respectively. The experimental measurements with the corresponding core radii $R_{\mathrm{core}} = 2.46 \pm 0.028$ fm and 1.13 ± 0.015 fm are shown in the shaded boxes. According to Fig. 1 of Ref. [17], strong resonances only reduce the height of the peak in the source function and do not affect its position. It can be inferred that the core source radius obtained in the “3 quarks” scenario after the ART stage is smaller than the corresponding core source extracted from experimental data within the given k_T interval. Therefore, as illustrated in Fig. 3, the “3 quarks” scenario already provides the largest size among the three configurations, the “Normal” and “Point-like” scenarios are too small to adequately describe the data. The effect of resonances on the source function is explained below.

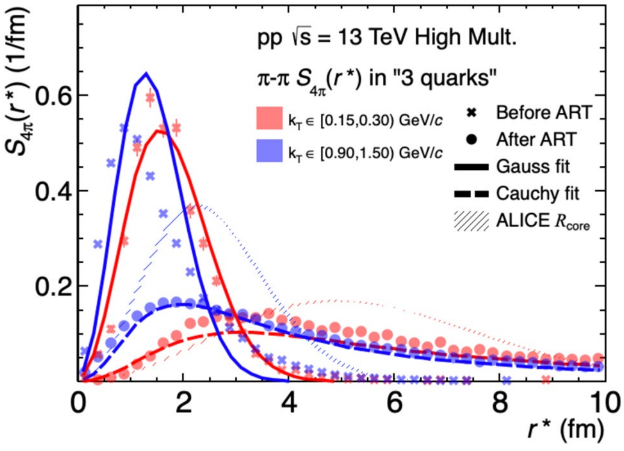

Fig. 4 (Color online) Source function in the $k_T \in [0.15, 0.3)$ and [0.9, 1.5) GeV/c intervals before- and after-ART stages within the “3 quarks” AMPT model. Fitting with Gaussian and Cauchy functions are represented by solid and dashed lines, respectively. The shaded bands are the core radii from Ref. [17]

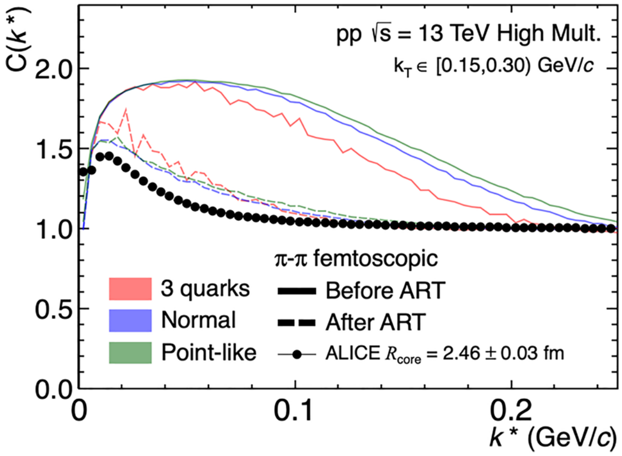

Fig. 5 (Color online) π-π correlation function in the k_T interval 0.15−0.30 GeV/c before and after the ART stages for three initial partonic distributions in the AMPT+CATS framework [70]

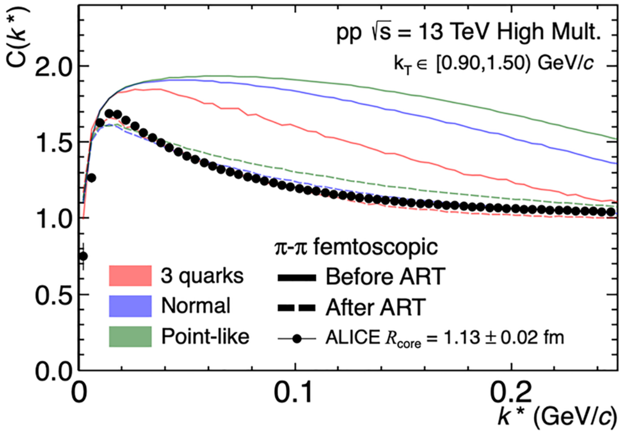

Fig. 6 (Color online) Same as Fig. 5, but for another k_T interval 0.90−1.50 GeV/c

3.3 π-π Correlation functions

To understand the impact of the source on the final correlation function, the simulation results are presented for three different initial partonic distributions before and after the ART stage using the aforementioned source functions and the accurate two-particle wave function from CATS [70]. The results are presented in Fig. 5 and Fig. 6 correspond to two examples k_T-intervals.

It can be observed that the correlation functions after the ART stage approximate the experimental data to a certain extent. By contrast, because the source distribution before the ART stage was concentrated in the small r^* region, the strength of the correlation function was higher than that observed in the experimental measurements. Considering only quantum statistical effects, the correlation function for two identical particles is given in Ref. [71] by $C(k^*) = 1 \pm \exp\left(-k^{*2}R^2\right)$, where the ± sign corresponds to the Bose–Einstein and Fermi–Dirac statistics. In this formula, the maximum value of the correlation function $C(k^*)$ equals 2 at $k^* = 0$, and decreases to 1 as k^* increases. However, because of the influence of long-range Coulomb interactions, the correlation function is significantly distorted for $k^* < 50$ MeV/c. For a large k^*, the correlation function approaches unity, and the rate of decrease is primarily determined by the shape of the source distribution. If the source is concentrated in the small r^* region, the correlation function decreases more slowly with k^*. Conversely, if the source is more widely distributed, the larger r^* regions, where the interactions are weaker, contribute more, leading to a larger dilution of the signal. It can also be observed that deviations in $C(k^*)$ between the three initial partonic conditions occur only at high k^* before ART, and are negligible at low k^* and after ART. This indicates that unlike azimuthal observables such as v_2 calculated in Refs. [44–46], $C(k^*)$ are less sensitive to initial geometrical conditions.

3.4 Impact of parton scattering cross-section on the source function

In addition to the initial position of the parton, the parton scattering cross-section σ_p, which reflects the probability of two partons interacting, also affects the source and final correlation functions, as previously discussed in Ref. [38]. In Fig. 7, the source function for the “3 quarks” scenario is presented for $\sigma_\mathrm{p} = 1.5$ mb and 10 mb. It was observed that σ_p significantly affected the source function before the ART stage. The results were similar for the other two initial partonic distributions. As σ_p increases, the probability of two-parton interactions increases, leading to a more dispersed parton and hadron distribution and, consequently, a wider source function. However, the results after the ART are almost unaffected by σ_p, indicating that the hadronic process plays a decisive role. Most of the initial effects were smeared or masked by hadronic scattering and resonance decay, which are discussed in the following section.

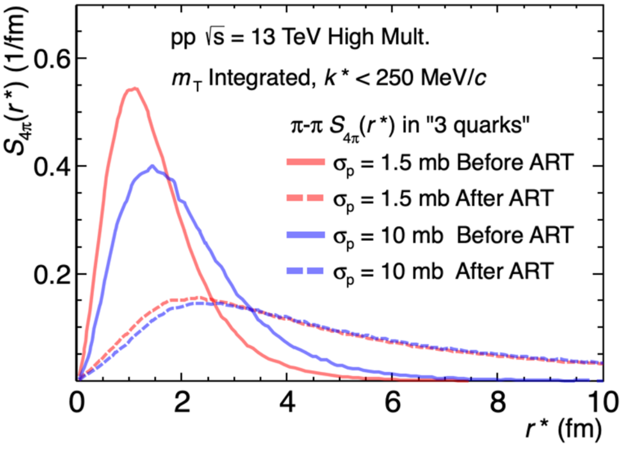

Fig. 7 (Color online) Source function for two-parton scattering cross-sections, $\sigma_\mathrm{p} = 1.5$ mb and 10 mb, before and after the ART stage in the “3 quarks” scenario

3.5 Impact of resonance and hadronic scattering on the source function

The hadronic interaction in AMPT and ART is dominated by two mechanisms: short-lived strongly decaying resonances and hadronic rescattering, including both elastic and inelastic processes. In Fig. 8 compared to the case where rescattering is turned off, the r^* distribution is wider when rescattering is on for all three initial conditions. This agrees with the expectation that the generated hadrons undergo adequate hadronic scattering, causing the entire system to expand outward. The long tail persists even when rescattering is off, suggesting a contribution from resonance decay.

As mentioned in Sect. 2, the source function has two main components: primordial particles produced in collisions, which are well described by a Gaussian distribution with width R_core (the core part), and a non-Gaussian contribution, represented by an exponential tail, mainly arising from short-lived resonances. A previous study showed that the Statistical Hadronization Model (SHM) [23] combined with EPOS [28] can accurately reproduce the tail part measured in ALICE [17, 18]. Using this approach, the core of the source was separated from the “resonance halo”.

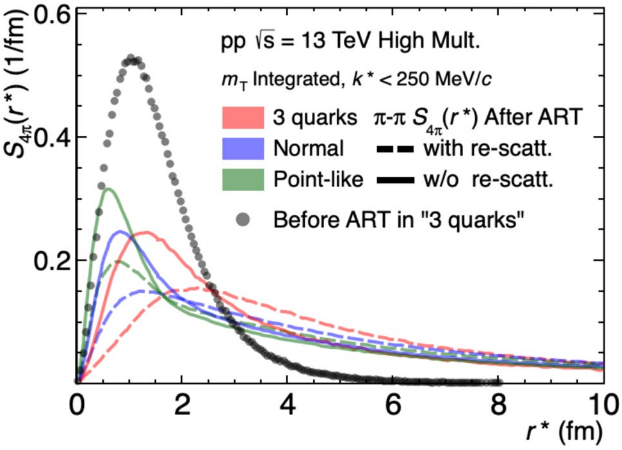

Fig. 8 (Color online) Source function, with and without hadronic rescattering, after the ART stage for three initial partonic distributions

Table 1 List of resonances contributing to the yield of π in HM pp collisions at $\sqrt{s} = 13$ TeV. The left column is from Ref. [17], calculated using the THERMAL-FIST package, while the right column shows the AMPT results without kinematic cuts

	SHM fraction (%)	“3 quarks” fraction (%)
Primordial	28.0	46.3
Strong resonances	72.0	53.7
Resonances		
$\rho(770)^0$	9.0	6.8
$\rho(770)^+$	8.7	13.9
$\omega(782)$	7.7	6.2
$K^*(892)^+$	2.3	4.3
$\bar{K}^*(892)^0$	2.6	4.2
$b_1(1235)^0$	1.9	-
$a_2(1320)^+$	1.5	-
η	1.5	19.9
$a_1(1260)^+$	1.4	-
$f_2(1270)$	1.4	-
$a_0(980)^+$	1.4	-
$h_1(1170)$	1.2	-

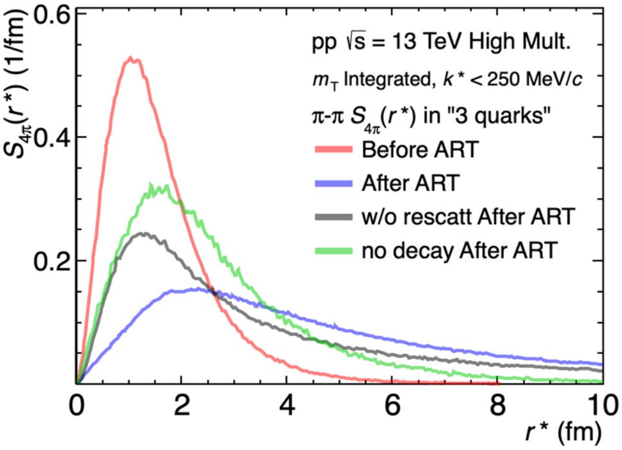

Fig. 9 (Color online) Source functions at four scenarios in the “3 quarks” AMPT. The black and green lines represent the results after ART, with the black line indicating no hadronic rescattering but including resonance decay, and the green line indicating no resonance decay but including hadronic rescattering. See the text for details

In the SHM calculation, only the decay products of short-lived resonances that contributed at least 1% were considered. As shown in Table 1, 28% of the charged pions are primordial, whereas 72% originate from resonance. However, in AMPT, several decay channels are not included, leading to a different fraction compared to the SHM calculation. There are ongoing efforts to incorporate production and annihilation channels into the ART stage [72], and a more thorough description of the resonances remains to be explored. Despite the differences in the resonance components and fractions, the qualitative impact of FSIs on the source is shown in Fig. 9. Four scenarios were investigated: before ART, after ART, after ART without the rescattering process, and after ART without resonance decay but with hadronic rescattering. The total ART contribution (blue) can be decomposed into the resonance (black) and hadronic rescattering (green) components. When no resonances contribute to the pions (green), the tail of the relative source function is significantly shorter than that of the gray function, which extends up to 30 fm.

3.6 Final source function and m_T-scaling

In principle, the standard method for subtracting the resonance contribution from the total source function and extracting R_{core} follows Eq. (4) in Ref. [18], which employs Gaussian fitting of $S_{\text{total}}(r^*)$ to decompose the primordial and resonance components. However, the applicability of this approach to the AMPT framework remains to be determined.

In the present study, we employed an alternative method. A schematic representation of the space-time dynamics is shown in Fig 2. Collisions with a given initial distribution (panel a) first proceed through the ZPC stage (green dashed circles). After the coalescence process, hadrons are formed (blue dashed circles), representing the stage before ART. To understand the core source function, the default resonance decays in the ART are fully turned off, and their contributions are excluded, matching the original definition of the core source and scenario described in Ref. [43]. Subsequently, the emission time parameter τ is introduced. The generated hadrons are forced to travel along their original momentum directions for τ fm/c without any hadronic interactions, resulting in an increase in the core source radii by $\vec{\beta}\tau$ fm ($\vec{\beta}$ is the particle velocity) in the spatial coordinates (panel b). For comparison, the default ART process, including hadronic interactions (red dashed circle), was also studied with a possible boost, where τ can be zero (panel c) or nonzero (panel d).

Figure 10 shows the r^* distribution (dots) and fitting results using Gaussians (lines) in the k_T interval of 0.15–0.3 GeV/c. The emission time parameter $\tau = 1.5$ fm/c was computed using the weighted abundances and lifetimes of the resonances considered in Ref. [17]. As expected, the average radius after ART (red) was larger than that before ART (blue). The fittings worked approximately despite minor inaccuracies. Notably, the results after ART were highly compatible with the ALICE results [17], indicating the validity of the model.

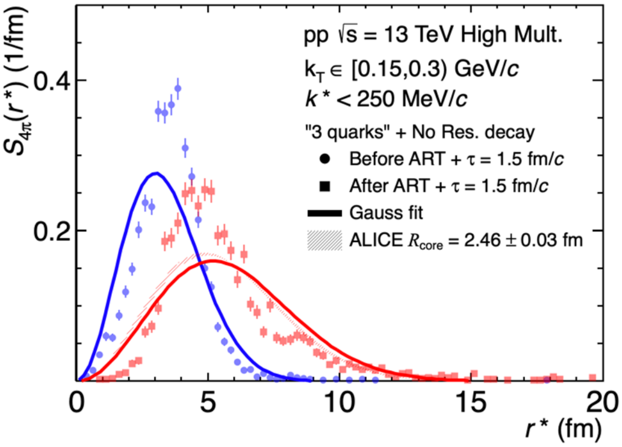

Fig. 10 (Color online) Fitting results for the r^* distribution in the $k_{\rm T} \in [0.15, 0.3]$ GeV/c. The blue and red markers represent results before and after the ART stage, respectively, with $\tau = 1.5$ fm/c. The shadow band represents the source distribution extracted by ALICE [17]

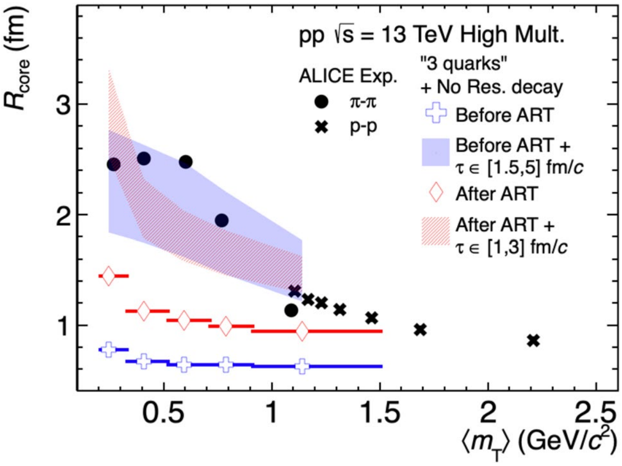

Fig. 11 (Color online) $m_{\rm T}$-scaling behavior of $R_{\rm core}$ in AMPT is shown for four emission scenarios (see the text for details) and is compared with the ALICE results (solid markers)

Based on the fitting results, the $R_{\rm core}$ values in each $k_{\rm T}$ interval are extracted for four different scenarios: (i) before ART without further boost, (ii) before ART with a boost of $\tau \in [1.5, 5]$ fm/c, (iii) after ART without boost, and (iv) after ART with a boost of $\tau \in [1, 3]$ fm/c. In (ii), the upper limit originates from the general assumption that resonances with $c\tau_{\rm res} > 5$ fm are long-lived, whereas in (iv), the τ values are deliberately reduced to approximately match the results of (ii). Figure 11 shows the $m_{\rm T}$-scaling behavior of the $R_{\rm core}$. All four cases are in line with the expectation that the source radii decrease as $m_{\rm T}$ increases, roughly following the power-law relationship [17]: $R_{\rm core} = a + b \cdot \langle m_{\rm T} \rangle^c$. This can be understood in terms of collectivity generated during the partonic stage. Compared with the ALICE measurements (solid dots), the original AMPT sources (i) and (iii) without additional boosting were systematically smaller, whereas the modified cases of (ii) and (iv) were in good agreement with the data in the low $m_{\rm T}$ ranges. Note that the ALICE results also exhibit a plateau at $m_{\rm T} < 0.5$ GeV/c^2, which can be interpreted as a limitation on the system size in pp collisions. However, this feature was not observed in AMPT, which instead followed a power-law increasing trend. Generally, AMPT provides a good environment to reveal the mechanisms behind the system size and $m_{\rm T}$-scaling; however, further investigation is required to understand the detailed behaviors.

4 Summary

This study investigated the pion emission source in high-multiplicity pp collisions at $\sqrt{s} = 13$ TeV using the AMPT model with different initial partonic distributions, including one with a subnucleon structure. The source functions and corresponding correlation functions were calculated, with the latter obtained using a precise two-particle FSI from the CATS framework. Results showed that the initial partonic distribution influences the source size, with the "3 quarks" mode generating a relatively larger radius owing to its larger initial spatial distribution. $k_{\rm T}$ dependence was observed, and the partonic scattering cross-section also played a role. However, in terms of the correlation function, the initial effects were largely smeared by FSIs. To understand the final-state dynamics, two main components, resonance decay and hadronic scattering, were carefully studied. The long tail in the source function is attributed to resonance. After tuning the decay process, the core source radius $R_{\rm core}$ can be extracted. Clear $m_{\rm T}$-scaling behavior was observed, and with an appropriate emission time, $R_{\rm core}$ in AMPT can reproduce the ALICE measurements well, providing new insights into the space-time characteristics, particle generation mechanisms in pp collisions, and potential improvements to the AMPT model.

In future studies, the resonance decay channels in the ART should be updated. The relationship between the radial (anisotropic) flow and the source function must be quantified. Studies on other particle species (e.g., p-p and K-p pairs) and source functions in multiple dimensions would also be valuable for a better understanding of experimental measurements.

Acknowledgements We are grateful to the femTUM group, led by Laura Fabbietti, for the enlightening discussions and suggestions, particularly to Maximilian Korwieser and Dimitar Mihaylov.

Author Contributions All authors contributed to the study conception and design. Material preparation, data collection, and analysis were performed by Dong-Fang Wang and Mei-Yi Chen. The first draft of the manuscript was written by Dong-Fang Wang and all authors commented on previous versions of the manuscript. All authors read and approved the final manuscript.

Data Availability The data that support the findings of this study are openly available in Science Data Bank at https://cstr.cn/31253.11.sciencedb.21971 and https://doi.org/10.57760/sciencedb.21971.

Declarations

Conflict of interest Yu-Gang Ma is the editor-in-chief for Nuclear Science and Techniques and was not involved in the editorial review, or the decision to publish this article. All authors declare that there are no Conflict of interest.

References

1. M.A. Lisa, S. Pratt, R. Soltz et al., Femtoscopy in relativistic heavy ion collisions. Ann. Rev. Nucl. Part. Sci. **55**, 357–402 (2005). https://doi.org/10.1146/annurev.nucl.55.090704.151533. arXiv:nucl-ex/0505014
2. L. Fabbietti, V. Mantovani Sarti, O. Vazquez Doce, Study of the strong interaction among hadrons with correlations at the LHC. Ann. Rev. Nucl. Part. Sci. **71**, 377–402 (2021). https://doi.org/10.1146/annurev-nucl-102419-034438. arXiv:2012.09806
3. R.B. Griffiths, Consistent histories and the interpretation of quantum mechanics. J. Stat. Phys. **36**, 219–272 (1984). https://doi.org/10.1007/BF01015734
4. R. Lednicky, V.L. Lyuboshits, Final state interaction effect on pairing correlations between particles with small relative momenta. Sov. J. Nucl. Phys. **35**, 770 (1982)
5. R. Lednický, Finite-size effect on two-particle production in continuous and discrete spectrum. Phys. Part. Nuclei **40**, https://doi.org/10.1134/S1063779609030034
6. L. Adamczyk, The STAR Collaboration, Measurement of interaction between antiprotons. Nature **527**, 345–348 (2015). https://doi.org/10.1038/nature15724
7. J. Adam, D. Adamová, M.M. Aggarwal et al., One-dimensional pion, kaon, and proton femtoscopy in Pb–Pb collisions at $\sqrt{s_{\mathrm{NN}}} = 2.76$ TeV. Phys. Rev. C **92**, 054908 (2015). https://doi.org/10.1103/PhysRevC.92.054908
8. S. Acharya, D. Adamová, J. Adolfsson et al., Measuring $K^0_sK^{\pm}$ interactions using Pb–Pb collisions at $\sqrt{s_{\mathrm{NN}}} = 2.76$ TeV. Phys. Lett. B **774**, 64–77 (2017). https://doi.org/10.1016/j.physletb.2017.09.009
9. S. Acharya, D. Adamová, A. Adler et al., Kaon-proton strong interaction at low relative momentum via femtoscopy in Pb-Pb collisions at the LHC. Phys. Lett. B **822**, 136708 (2021). https://doi.org/10.1016/j.physletb.2021.136708
10. M. Gyulassy, S. Kauffmann, L.W. Wilson, Pion interferometry of nuclear collisions. I. Theory. Phys. Rev. C. **20**, 2267 (1979). https://doi.org/10.1103/PhysRevC.20.2267
11. A. Capella, A. Krzywicki, E.M. Levin, Pion interferometry and intermittency in heavy-ion collisions. Phys. Rev. D **44**, 704–716 (1991). https://doi.org/10.1103/PhysRevD.44.704
12. K. Aamodt, N. Abel, U. Abeysekara et al., Two-pion Bose-Einstein correlations in pp collisions at $\sqrt{s} = 900$ GeV. Phys. Rev. D **82**, 052001 (2010). https://doi.org/10.1103/physrevd.82.052001
13. K. Aamodt, A. Abrahantes Quintana, D. Adamová et al., Two-pion Bose-Einstein correlations in central Pb-Pb collisions at $\sqrt{s_{\mathrm{NN}}} = 2.76$ TeV. Phys. Lett. B **696**, 328–337 (2011). https://doi.org/10.1016/j.physletb.2010.12.053
14. M.G. Bowler, Extended sources, final state interactions and Bose-Einstein correlations. Zeitschrift für Physik C Aip Conf Proc **39**, 81–88 (1988). https://doi.org/10.1007/BF01560395
15. G. Colangelo, J. Gasser, H. Leutwyler, $\pi\pi$ scattering. Nucl. Phys. B **603**, 125–179 (2001). https://doi.org/10.1016/s0550-3213(01)00147-x
16. S.K. Adhikari, J.R.A. Torreão, Effective range expansion for the pion-pion system. Phys. Lett. B **123**, 452–454 (1983). https://doi.org/10.1016/0370-2693(83)90992-9
17. Common femtoscopic hadron-emission source in pp collisions at the LHC. (2023). arXiv: https://arxiv.org/abs/2311.14527
18. S. Acharya, D. Adamová, A. Adler et al., Search for a common baryon source in high-multiplicity pp collisions at the LHC. Phys. Lett. B **811**, 135849 (2020). https://doi.org/10.1016/j.physletb.2020.135849. arXiv:2004.08018
19. A. Kisiel, M. Gałażyn, P. Bożek, Pion, kaon, and proton femtoscopy in Pb–Pb collisions at $\sqrt{s_{\mathrm{NN}}} = 2.76$ TeV modeled in (3+1) D hydrodynamics. Phys. Rev. C **90**, 064914 (2014). https://doi.org/10.1103/PhysRevC.90.064914
20. A. Kisiel, Pion-kaon femtoscopy in Pb-Pb collisions at $\sqrt{s_{\mathrm{NN}}} = 2.76$ TeV modeled in (3+1)D hydrodynamics coupled to Therminator 2 and the effect of delayed kaon emission. Phys. Rev. C **98**, 044909 (2018). https://doi.org/10.1103/PhysRevC.98.044909
21. V.M. Shapoval, Yu.M. Sinyukov, Bulk observables in Pb–Pb collisions at $\sqrt{s_{\mathrm{NN}}} = 5.02$ TeV at the CERN Large Hadron Collider within the integrated hydrokinetic model. Phys. Rev. C **100**, 044905 (2019)
22. V. Shapoval, P. Braun-Munzinger, I. Karpenko et al., Femtoscopy correlations of kaons in Pb-Pb collisions at LHC within hydrokinetic model. Nucl. Phys. A **929**, 1–8 (2014). https://doi.org/10.1016/j.nuclphysa.2014.05.003
23. M. Chojnacki, A. Kisiel, W. Florkowski et al., THERMINATOR 2: THERMal heavy IoN generATOR 2. Comput. Phys. Commun. **183**, 746–773 (2012). https://doi.org/10.1016/j.cpc.2011.11.018
24. S. Acharya, D. Adamová, S.P. Adhya et al., Investigations of anisotropic flow using multiparticle azimuthal correlations in pp, p-Pb, Xe-Xe, and Pb-Pb collisions at the LHC. Phys. Rev. Lett. **123**, 142301 (2019). https://doi.org/10.1103/PhysRevLett.123.142301
25. S. Acharya, D. Adamová, G. Aglieri Rinella et al., Emergence of long-range angular correlations in low-multiplicity proton-proton collisions. Phys. Rev. Lett. **132**, 172302 (2024). https://doi.org/10.1103/PhysRevLett.132.172302
26. S. Acharya, ALICE Collaboration, Observation of partonic flow in proton-proton and proton-nucleus collisions. (2024). arXiv: https://arxiv.org/abs/2411.09323
27. W. Wu (for the ALICE Collaboration), Probing partonic collectivity in pp and p–Pb collisions with ALICE., talk given at IS2023 (2023). https://indico.cern.ch/event/1043736/contributions/5363771/
28. T. Pierog, I. Karpenko, J.M. Katzy et al., EPOS LHC: Test of collective hadronization with data measured at the CERN Large Hadron Collider. Phys. Rev. C **92**, 034906 (2015). https://doi.org/10.1103/PhysRevC.92.034906
29. M. Bleicher, E. Zabrodin, C. Spieles et al., Relativistic hadron-hadron collisions in the ultra-relativistic quantum molecular dynamics model. J. Phys. G: Nucl. Part. Phys. **25**, 1859–1896 (1999). https://doi.org/10.1088/0954-3899/25/9/308

30. S. Bass, Microscopic models for ultrarelativistic heavy ion collisions. Prog. Part. Nucl. Phys. **41**, 255–369 (1998). https://doi.org/10.1016/s0146-6410(98)00058-1
31. P. Li, J. Steinheimer, T. Reichert et al., Effects of a phase transition on two-pion interferometry in heavy ion collisions at $\sqrt{s_{\mathrm{NN}}}$ = 2.4-7.7 GeV. Sci. China Phys. Mechan. Astron. **66**, 232011 (2022). https://doi.org/10.1007/s11433-022-2041-8
32. P. Li, Y. Wang, Q. Li et al., Transport model analysis of the pion interferometry in Au+Au collisions at Ebeam=1.23 GeV/nucleon. Sci. China Phys., Mech. Astron. **66**, 222011 (2022). https://doi.org/10.1007/s11433-022-2026-5
33. L.M. Fang, Y.G. Ma, S. Zhang, Azimuthal-sensitive three-dimensional HBT radius in Au-Au collisions at E_{beam} = 1.23AGeV by the IQMD model. The Eur. Phys. J. A **58**, 81 (2022). https://doi.org/10.1140/epja/s10050-022-00722-w
34. L.M. Fang, Y.G. Ma, S. Zhang, Simulation of collective flow of protons and deuterons in Au+Au collisions at E_{beam}=1.23AGeV with the isospin-dependent quantum molecular dynamics model. Phys. Rev. C **107**, 044904 (2023). https://doi.org/10.1103/PhysRevC.107.044904
35. L.Y. Li, P. Ru, Y. Hu, Probing granular inhomogeneity of a particle-emitting source by imaging two-pion Bose-Einstein correlations. Nucl. Sci. Tech. **32**, 19 (2021). https://doi.org/10.1007/s41365-021-00853-7
36. S. Pratt, J. Sullivan, H. Sorge et al., Testing transport theories with correlation measurements. Nucl. Phys. A **566**, 103–114 (1994). https://doi.org/10.1016/0375-9474(94)90614-9
37. Z.W. Lin, C.M. Ko, S. Pal, Partonic effects on pion interferometry at the relativistic heavy-ion collider. Phys. Rev. Lett. **89**, 152301 (2002). https://doi.org/10.1103/physrevlett.89.152301
38. Z.W. Lin, 3D pion source functions from the AMPT model. J. Phys. G: Nucl. Part. Phys. **35**, 104138 (2008). https://doi.org/10.1088/0954-3899/35/10/104138
39. A. Ayala, S. Bernal-Langarica, I. Dominguez et al., Collision energy dependence of source sizes for primary and secondary pions at NICA energies. (2024). arXiv:2401.00619
40. M. Stefaniak, D. Kincses, Investigating the pion source function in heavy-ion collisions with the EPOS model. in *Photonics Applications in Astronomy, Communications, Industry, and High Energy Physics Experiments* 2020, 1158112 (2020). https://doi.org/10.1117/12.2580570
41. E. Khyzhniak, V. Semenova, N. Ermakov et al., Estimation of pion-emitting source in symmetric and asymmetric collisions using the UrQMD model. Epj Web Conf. **204**, 03017 (2019). https://doi.org/10.1051/epjconf/201920403017
42. N. Ermakov, G. Nigmatkulov, Modeling of two-particle femtoscopic correlations at top RHIC energy. J. Phys: Conf. Ser. **798**, 012055 (2017). https://doi.org/10.1088/1742-6596/798/1/012055
43. D. Mihaylov, J. González González, Novel model for particle emission in small collision systems. The Eur. Phys. J. C. **83**, 590 (2023). https://doi.org/10.1140/epjc/s10052-023-11774-7
44. L. Zheng, G.H. Zhang, Y.F. Liu et al., Investigating high energy proton proton collisions with a multi-phase transport model approach based on PYTHIA8 initial conditions. The Eur. Phys. J. C. **81**, 755 (2021). https://doi.org/10.1140/epjc/s10052-021-09527-5
45. X.L. Zhao, Z.W. Lin, L. Zheng et al., A transport model study of multiparticle cumulants in pp collisions at 13 TeV. Phys. Lett. B **839**, 137799 (2023). https://doi.org/10.1016/j.physletb.2023.137799
46. L. Zheng, L. Liu, Z.W. Lin et al., Disentangling the development of collective flow in high energy proton proton collisions with a multiphase transport model. The Eur. Phys. J. C. **84**, 1029 (2024). https://doi.org/10.1140/epjc/s10052-024-13378-1
47. Z.W. Lin, C.M. Ko, B.A. Li et al., Multiphase transport model for relativistic heavy ion collisions. Phys. Rev. C **72**, 064901 (2005). https://doi.org/10.1103/PhysRevC.72.064901
48. Z.W. Lin, L. Zheng, Further developments of a multi-phase transport model for relativistic nuclear collisions. Nucl. Sci. Tech. **32**, 113 (2021). https://doi.org/10.1007/s41365-021-00944-5
49. W.J. Dong, X.Z. Yu, S.Y. Ping et al., Study of baryon number transport dynamics and strangeness conservation effects using Ω-hadron correlations. Nucl. Sci. Tech. **35**, 120 (2024). https://doi.org/10.1007/s41365-024-01464-8
50. X.H. Jin, J.H. Chen, Z.W. Lin et al., Explore the QCD phase transition phenomena from a multiphase transport model. Sci. China Phys. Mech. Astron. **62**, 11012 (2019). https://doi.org/10.1007/s11433-018-9272-4
51. S.Y. Tang, L. Zheng, X.M. Zhang et al., Investigating the elliptic anisotropy of identified particles in p-Pb collisions with a multiphase transport model. Nucl. Sci. Tech. **35**, 32 (2024). https://doi.org/10.1007/s41365-024-01387-4
52. H. Wang, J.H. Chen, Y.G. Ma et al., Charm hadron azimuthal angular correlations in Au+Au collisions at $\sqrt{s_{\mathrm{NN}}}$ = 200 GeV from parton scatterings. Nucl. Sci. Tech. **30**, 185 (2019). https://doi.org/10.1007/s41365-019-0706-z
53. T.T. Wang, Y.G. Ma, S. Zhang, Calculation of momentum correlation functions between π, K, and p for several heavy-ion collision systems at $\sqrt{s_{NN}}$=39 GeV. Phys. Rev. C **109**, 024912 (2024). https://doi.org/10.1103/PhysRevC.109.024912
54. Y.G. Ma, Effects of α-clustering structure on nuclear reaction and relativistic heavy-ion collisions. Nuclear Techniques (in Chinese) **46**, 080001 (2024). https://doi.org/10.11889/j.0253-3219.2023.hjs.46.080001
55. Q. Chen, G.L. Ma, J.H. Chen, Transport model study of conserved charge fluctuations and QCD phase transition in heavy-ion collisions. Nuclear Techniques (in Chinese) **46**, 040013 (2024). https://doi.org/10.11889/j.0253-3219.2023.hjs.46.040013
56. X.N. Wang, M. Gyulassy, HIJING: A Monte Carlo model for multiple jet production in pp, pA and AA collisions. Phys. Rev. D **44**, 3501–3516 (1991). https://doi.org/10.1103/PhysRevD.44.3501
57. M. Gyulassy, X.N. Wang, Hijing 1.0: A Monte Carlo program for parton and particle production in high energy hadronic and nuclear collisions. Comp. Phys. Commun. **83**, 307–331 (1994). https://doi.org/10.1016/0010-4655(94)90057-4
58. B. Zhang, ZPC 1.0.1: a parton cascade for ultrarelativistic heavy ion collisions. Comp. Phys. Commun. **109**, 193–206 (1998). https://doi.org/10.1016/S0010-4655(98)00010-1
59. B.A. Li, C.M. Ko, Formation of superdense hadronic matter in high energy heavy-ion collisions. Phys. Rev. C **52**, 2037–2063 (1995). https://doi.org/10.1103/PhysRevC.52.2037
60. Y.C. He, Z.W. Lin, Improved quark coalescence for a multi-phase transport model. Phys. Rev. C **96**, 014910 (2017). https://doi.org/10.1103/physrevc.96.014910
61. A. Collaboration, Unveiling the strong interaction among hadrons at the LHC. Nature **588**, 232–238 (2020). https://doi.org/10.1038/s41586-020-3001-6
62. T. Csörgő, B. Lörstad, J. Zimányi, Bose-Einstein correlations for systems with large halo. Zeitschrift für Physik C: Aip Conf Proc **71**, 491–497 (1996). https://doi.org/10.1007/bf02907008
63. A.M. Sirunyan, A. Tumasyan, W. Adam et al., Bose-Einstein correlations of charged hadrons in proton-proton collisions at $\sqrt{s}$ = 13 TeV. J. High Energy Phys. **2020**, 14 (2020). https://doi.org/10.1007/jhep03(2020)014
64. G. Aad, B. Abbott, J. Abdallah et al., Two-particle Bose-Einstein correlations in pp collisions at $\sqrt{s}$ = 0.9 and 7 TeV

measured with the ATLAS detector. The Eur. Phys. J. C **75**, 466 (2015). https://doi.org/10.1140/epjc/s10052-015-3644-x

65. A.M. Sirunyan, A. Tumasyan, W. Adam et al., Bose-Einstein correlations in pp, p–Pb, and Pb–Pb collisions at $\sqrt{s_{\mathrm{NN}}} = 0.9$–7 TeV. Phys. Rev. C **97**, 064912 (2018). https://doi.org/10.1103/PhysRevC.97.064912
66. T. Csörgő, S. Hegyi, W.A. Zajc, Bose-Einstein correlations for Lévy stable source distributions. Eur. Phys. J. C **36**, 67–78 (2004). https://doi.org/10.1140/epjc/s2004-01870-9
67. K. Aamodt, A. Abrahantes Quintana, D. Adamová et al., Femtoscopy of pp collisions at $\sqrt{s} = 0.9$ and 7 TeV at the LHC with two-pion Bose-Einstein correlations. Phys. Rev. D **84**, 112004 (2011). https://doi.org/10.1103/PhysRevD.84.112004
68. K. Aamodt, A. Abrahantes Quintana, D. Adamová et al., Two-pion Bose-Einstein correlations in central Pb–Pb collisions at $\sqrt{s_{\mathrm{NN}}} = 2.76$ TeV. Phys. Lett. B **696**, 328–337 (2011). https://doi.org/10.1016/j.physletb.2010.12.053
69. S. Acharya, D. Adamová, G. Aglieri Rinella et al., Exploring the strong interaction of three-body systems at the LHC. Phys. Rev. X **14**, 031051 (2024). https://doi.org/10.1103/PhysRevX.14.031051
70. D.L. Mihaylov, V. Mantovani Sarti, O.W. Arnold et al., A femtoscopic correlation analysis tool using the Schrödinger equation (CATS). Eur. Phys. J. C. **78**, 394 (2018). https://doi.org/10.1140/epjc/s10052-018-5859-0
71. K. Yagi, T. Hatsuda, Y. Miake, *Quark-gluon plasma: From big bang to little bang*, Vol. 23, (2005)
72. Y. Oh, Z.W. Lin, C.M. Ko, Deuteron production and elliptic flow in relativistic heavy ion collisions. Phys. Rev. C **80**, 064902 (2009). https://doi.org/10.1103/PhysRevC.80.064902